Journal of Alloys and Compounds 698 (2017) 944–956

Contents lists available at ScienceDirect

Journal of Alloys and Compounds

journal homepage: http://www.elsevier.com/locate/jalcom

Targeting low-cost type-II heterostructures: Synthesis, structure and photoreactivity

Arik Kar [a, *], Sumanta Sain [b], David Rossouw [c], Benjamin R. Knappett [a], Swapan Kumar Pradhan [b], Gianluigi A. Botton [c], Andrew E.H. Wheatley [a, **]

[a] Department of Chemistry, University of Cambridge, Lensfield Road, Cambridge, CB2 1EW, UK
[b] Materials Science Division, Department of Physics, The University of Burdwan, Golapbag, Burdwan, West Bengal, 713 104, India
[c] Department of Materials Science and Engineering, Brockhouse Institute for Materials Research and Canadian Centre for Electron Microscopy, McMaster University, Hamilton, Ontario, L8S 4L8, Canada

ARTICLE INFO

Article history:
Received 10 June 2016
Received in revised form
2 December 2016
Accepted 14 December 2016
Available online 18 December 2016

Keywords:
SnO_2 nanosphere
PbS nanocube
Rietveld refinement
Heterostructure
Photochemistry

ABSTRACT

One design strategy by which to iterate the photocatalytic efficiency of semiconducting nanomaterials for harvesting solar energy involves the synthesis of type-II heterostructured materials. In this article, a straightforward, facile and environmentally benign route to heterostructures in which SnO_2 nanospheres are capped by PbS nanocubes is reported. It offers to address current limitations to photocatalytic efficiency brought about by electron-hole recombination and narrow photoresponsive ranges in many existing systems. PbS nanocubes are grown in the presence of preformed SnO_2 nanospheres by functionalizing the surface of the latter using cetyltrimethylammonium bromide (CTAB). Heterostructure formation is confirmed by X-ray diffraction (XRD), Raman spectroscopy, X-ray photoelectron spectroscopy (XPS), Brunauer-Emmett-Teller (BET) surface area analysis, and transmission electron microscopy (TEM) analysis. Rietveld refinement has been exploited to simultaneously elucidate the atomic and microstructures of these materials, allowing the quantitative determination of particle structure and stability. The combination of narrow band-gap semiconductor (PbS) and wide band-gap semiconductor (SnO_2) endows the heterostructured nanomaterial with potential as a photocatalyst and, in the degradation of Rhodamine B (RhB) dye under solar simulation, it showed superior photocatalytic activity to that of its separate SnO_2 and PbS components. A strong type-II interaction is demonstrated by the heterostructure and a charge separation mechanism has been utilized to clarify this behaviour.

1. Introduction

The use of more than 8000 types of dye in a range of industries is long established and applications continue to develop [1]. For example, dyes have lately achieved prominence as metal-free catalysts for transformations achieved in continuous microflow [2]. However, in spite of their immense importance, dyes suffer from significant toxicological and environmental drawbacks [1,3]. One response has been the direction of efforts towards their chemical passivation, with photocatalysis gaining traction as a 'green' technique with enormous potential for achieving this [4]. Semiconducting metal oxides can degrade a variety of dyes under UV–Vis light irradiation and to this end many types of such oxide have been developed [5]. Nevertheless, enhancing the photocatalytic effectiveness of such systems remains a considerable challenge on account of poor quantum yields caused by the fast recombination of photogenerated electrons and holes [6].

Recent work has shown that the heterostructuring of semiconductors represents one route by which to improve their photochemical properties. This has led to new materials based on oxide-oxide [7–12] and oxide-sulfide [13–15] combinations. However, while such recently reported systems have offered improved photocatalytic capabilities they have also exhibited significant limitations. These have included (i) the agglomeration of core nanoparticles, (ii) preferential formation of separate sets of individually monometallic particles, (iii) incomplete coverage of the core by the second semiconductor, (iv) inappropriate charge separation, and/or (v) still only moderate photoresponsive ranges. One promising avenue by which to potentially overcome these

* Corresponding author.
** Corresponding author.
E-mail address: ak899@cam.ac.uk (A. Kar).

http://dx.doi.org/10.1016/j.jallcom.2016.12.167

problems involves the fabrication of SnO_2-based core@shell heterostructures. These promise to use a commercially appealing oxides (core) in conjunction with a second semiconductor (shell) to raise photocatalytic efficiency by increasing charge separation and extending the photoresponsive range of the catalyst into the visible region of the electromagnetic spectrum. However, a survey of the limited literature [15,16] in the field shows that the goal of fabricating compelling SnO_2-based core@shell heterostructures remains elusive. For example, in terms of oxide-sulfide combinations, SnO_2-based heterostructures containing PbS are, to the best of our knowledge, unreported. We have therefore sought to develop a SnO_2@PbS system. The desirability of such a combination is based upon there being a large band gap difference (approximately 3.2 eV) between the two materials. This offers increased charge separation and promises enhanced electrical, optical, electrochemical, photocatalytic and gas sensing properties. It also promises a type-II system that exhibits charge separation that is improved relative to that seen in either component individually. This would dervive from the heterojunction between SnO_2 and PbS hampering the recombination of photoinduced charge carriers [17].

This article examines the formation of a type-II system in which preformed SnO_2 supports PbS. A simple solution approach is used. It involves only relatively inexpensive substrates [18] under facile conditions to make SnO_2 nanospheres (NSs) which are then coated with PbS nanocubes (NCs; Fig. 1). The structure, morphology and electronic properties of the heterostructured product are comprehensively elucidated by X-ray diffraction (XRD)/Rietveld refinement, Raman spectroscopy, X-ray photoelectron spectroscopy (XPS), Brunauer-Emmett-Teller (BET) surface area analysis, and transmission electron microscopy (TEM) analysis. Rietveld refinement has been employed to probe lattice strain, lattice parameters and relative phase abundances. Detailed atomic structure modeling has also been undertaken for each phase. The photocalalytic activity of an as-synthesized heterostructured material is estimated in term of the degradation of Rhodamine B (RhB) dye. The effects of crystallinity and specific surface area on the photocatalytic activity of the new heterostructured material are discussed. An existing mechanistic proposal [19] is able to explain the photocatalytic behaviour observed.

2. Experimental

2.1. Materials and preparation

2.1.1. General synthetic and analytical details

Chemicals were obtained from Sigma-Aldrich (analytical grade reagents, HPLC grade solvents) and used without further purification. Aqueous solutions used HPLC water (Millipore). PbS NCs were prepared using a literature method [19].

2.1.2. SnO_2 nanosphere synthesis

$SnCl_4 \cdot 5H_2O$ (0.351 g, 1.0 mmol) was dissolved in water (25 ml) and a solution of cetyltrimethylammonium bromide (CTAB, 0.365 g, 1.0 mmol) in water (5 ml) was added. The mixture was stirred for 1 h to give a colourless solution. NaOH (0.8 g, 20.0 mmol) was dissolved in water (10 ml) and 10 ml of EtOH was added. This solution was added dropwise to the stirred $SnCl_4 \cdot 5H_2O$ solution to give a white precipitate, which dissolved once a pH of 11–12 was reached. The solution was heated in a microwave reactor (CEM, Discover, operating at 300 W) at 110 °C for 5 min to give a white colloidal suspension. Centrifugation and washing with water (2 × 25 ml) and absolute EtOH (3 × 25 ml) before drying at 60 °C in air gave SnO_2 NSs.

2.1.3. SnO_2 nanosphere/PbS nanocube heterostructure synthesis

A soft chemical process [20] was used in which SnO_2 NSs (0.015 g, 0.1 mmol) [21] were dispersed in water (25 ml) by ultrasonication. CTAB (0.036 g, 0.1 mmol) was added with stirring. The resulting dispersion was slowly heated to 50 °C, kept at this temperature for 2 h. It was then left to cool to room temperature, during which time flocculation occurred. A 5 ml aqueous solution of $Na_2S \cdot 9H_2O$ (0.024 g, 0.1 mmol) was added dropwise and the resulting mixture was stirred for 30 min. Finally, a 5 ml aqueous solution of $Pb(NO_3)_2$ (0.033 g, 0.1 mmol) was added dropwise and the mixture stirred for 2 h at room temperature. The product was obtained by centrifugation. Washing with water (2 × 25 ml) and absolute EtOH (3 × 25 ml) before vacuum drying for 6 h gave a grey powder. See Fig. 1.

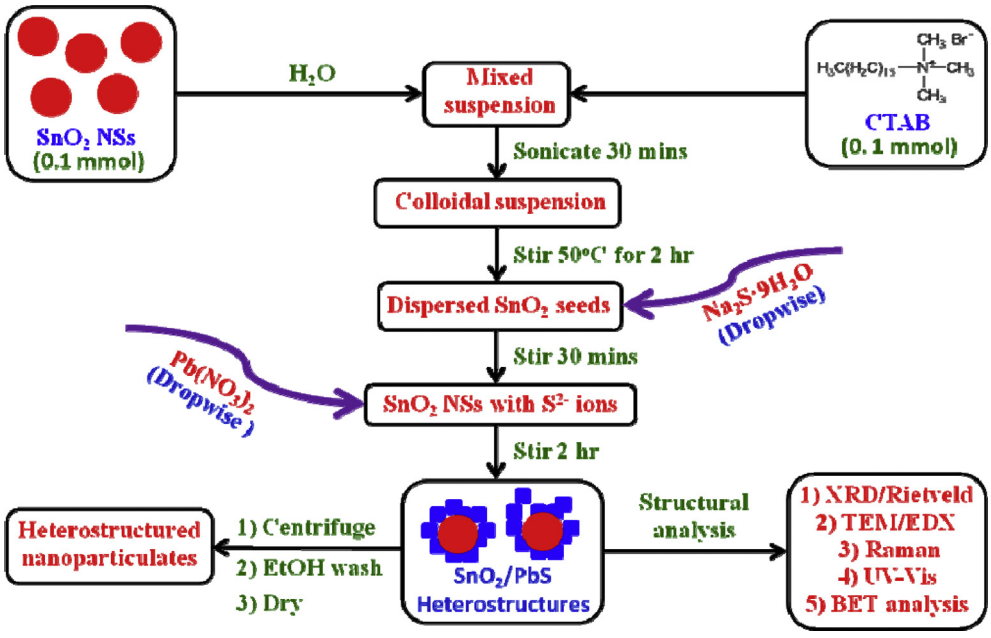

Fig. 1. Synthetic scheme for the preparation of SnO_2/PbS heterostructures.

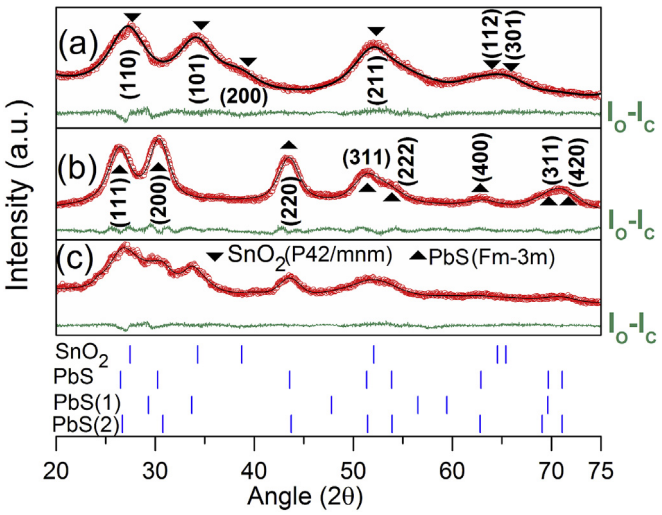

Fig. 2. Experimental (red circles) and simulated (black lines) XRD patterns of (a) SnO_2 NSs, (b) PbS NCs and (c) SnO_2/PbS heterostructures. Peaks are indexed according to blue markers (|) and PbS(1) and PbS(2) represent cubic PbS phases with different lattice parameters. Difference patterns between observed and calculated intensity (I_O-I_C) are shown in green. (For interpretation of the references to colour in this figure legend, the reader is referred to the web version of this article.)

2.2. Characterization

2.2.1. X-ray diffraction (XRD)

XRD profiles were recorded using Ni-filtered CuKα radiation from a highly stabilized and automated PAN-analytical X-ray generator operated at 40 kV and 40 mA. The X-ray generator was coupled with a PW3071/60 bracket goniometer for sample mounting. Step-scan data (step size 0.02° 2θ, counting time 2 s/step) were recorded for 20°–75° 2θ.

2.2.2. Rietveld analysis

Rietveld refinement [22] utilized MAUD [23] to refine (micro) structural parameters using an analytical function, the intensity of which was directly related to the structure of each phase [24]. XRD peaks were quite broad and not perfectly Gaussian, leading to the use of pseudo Voigt (pV) as a profile function [25,26] that accounted for broadening due both to particle size and strain. Shape parameters, e.g. full-width-at-half-maximum values (FWHM) and the Gaussianity for true line broadening profile functions, were generated by refining crystallite size and microstrain values. The background was simulated using a four-degree polynomial. This procedure has previously been shown to be appropriate to systems of the type analyzed here [27,28].

2.2.3. Transmission electron microscopy (TEM)

A Technai 20 TEM was used to screen nanoparticle size and morphology. Data were analyzed using Digital Micrograph 3.6.5. Both high-angle annular dark field (HAADF) imaging and energy-dispersive X-ray (EDX) techniques were utilized to characterize individual heterostructures. High-resolution (HR) electron microscopy was performed using a Titan 80-300 TEM. Sample preparation was by droplet coating of ethanolic suspensions on carbon-coated Cu grids (Agar Scientific, 300 mesh).

2.2.4. Raman spectroscopy

Data were collected at room temperature on a Thermo Scientific DXR Raman microscope using a helium-neon laser with an excitation wavelength of 532 nm (laser power 10 mW).

2.2.5. X-ray photoelectron spectroscopy (XPS)

XPS measurements were obtained using a Thermo Scientific K-Alpha system. Binding energy was calibrated internally with respect to the C1s line.

2.2.6. UV–vis spectroscopy

UV–Visible absorption spectra were measured in ethanolic solution on a UV–vis spectrophotometer (Perkin Elmer LAMBDA 265).

2.2.7. Brunauer-Emmett-Teller (BET) surface area analysis

BET surface areas were analyzed by nitrogen adsorption in a Tristar 3000 analyzer. Samples were degassed at 77 K before measurements were commenced. Surface areas were determined by a multipoint BET method using the adsorption data in the P/P_0 range 0.0–1.0 (where P and P_0 are the equilibrium and the saturation pressure of adsorbates at the temperature of adsorption).

2.2.8. Photocatalytic measurements

The room temperature degradation of aqueous Rhodamine B under simulated solar irradiation was studied without using sacrificial reagents. Typically, 5.0 mg of catalyst was added to 25 ml of a 1.0×10^{-5} M aqueous solution of RhB (pH 7), and the mixture stirred in the dark for 30 min to allow dye adsorption to the catalyst surface [29]. A 3.0 ml aliquot of the mixture was centrifuged and the absorption of the dye therein determined to obtain dye concentration before photocatalysis (C_0). The remaining solution was irradiated with a 300 W xenon lamp (Solar Simulator model LSO306, AM 1.5 G filter, 1 sun illumination at 100 mW cm^{-2}). Degradation of the RhB absorption maximum at 555 nm was monitored using a UV–vis spectrophotometer (Perkin Elmer LAMBDA 265) to obtain the concentration (C) of dye as a function of time in subsequent aliquots. Use of an ice bath prevented evaporation during catalysis and avoided degradation due to heating. Degradation and apparent quantum yield (φ_x) were calculated according to:

$$\text{Degradation}\ (\%) = (1 - C/C_0) \times 100 \quad (1)$$

$$\varphi_x = \pm(d[x]/dt)/d[h\nu]_{inc}/dt \quad (2)$$

where $d[x]/dt$ is the rate of change of the concentration of RhB and $d[h\nu]_{inc}/dt$ is the total optical power impinging on the sample [30].

Hydroxyl radicals (OH•) produced during photocatalysis were estimated by fluorescence spectroscopy using terephthalic acid (TA) as a probe molecule. Catalyst (5.0 mg) was dispersed in an aqueous solution of 30 ml of TA (5×10^{-4} M) and NaOH (2×10^{-3} M). The resulting suspension was exposed to simulated solar radiation and at regular intervals 3.0 ml of the suspension was

Table 1
(Micro)structural parameters for SnO_2 NSs.

Sp. Gr.	Lattice parameters (Å)		Particle size (nm)	r.m.s. microstrain	Atomic coordinates of oxygen			Oxygen occupancy
	a	c			x	y	z	
$P4_2/mnm$	4.8058	3.2622	2.19	1.2×10^{-3}	0.306	0.305	0	0.996

Table 2
(Micro)structural parameters for SnO_2/PbS heterostructures.

Compounds	Vol. (%)	Lattice parameters (Å)		Particle size (nm)	r.m.s. microstrain	Atomic coordinates of oxygen		
		a	c			x	y	z
SnO_2 nanosphere ($P4_2/mnm$)	61.42	4.8937	3.0993	4.95	0.0269	0.334	0.297	0
PbS(1)	16.60	5.4621		Anisotropic particle size (nm)	Planar direction	r.m.s. microstrain		
(Fm-3m)				68.22	(111)	0.0607		
				5.57	(200)	0.0146		
				67.12	(220)	0.0504		
				55.84	(311)	0.0563		
				68.22	(222)	0.0607		
				5.57	(400)	0.0146		
				66.39	(331)	0.0599		
				56.13	(420)	0.0338		
				60.02	(422)	0.0578		
PbS(2)	21.98	5.9894		46.16	(111)	0.1388		
(Fm-3m)				3.75	(200)	0.0007		
				18.76	(220)	0.0214		
				41.56	(311)	0.0908		
				46.16	(222)	0.1388		
				3.75	(400)	0.0007		
				33.69	(331)	0.1081		
				12.22	(420)	0.0170		
				43.10	(422)	0.1075		

collected and centrifuged. The maximum fluorescence emission intensity of the supernatant was measured with an excitation wavelength of 315 nm. This method relies on the fluorescence at 425 nm of 2-hydroxyterephthalic acid (TAOH) and was undertaken using an Edinburgh Instruments FLS980 photoluminescence spectrometer.

3. Results and discussion

3.1. XRD phase identification

Observed and Rietveld simulated XRD patterns for SnO_2 NSs are shown in Fig. 2a. Peaks are unambiguously identified and indexed using reflections from tetragonal SnO_2 (ICSD 154960, space group: $P4_2/mnm$, $a = 4.7331$ Å, $c = 3.1815$ Å). Signal breadth implied very small particle sizes and significant lattice strain. Rietveld refinement yielded mean particle sizes (MPSs) for individual nanocrystallites by considering the line broadening of reflections across the entire angular range studied. Results suggested a mean particle size of 2.19 nm and a r.m.s lattice strain of 1.2×10^{-3} (Table 1). Analysis of oxygen atom occupancy in the SnO_2 lattice revealed oxygen deficiencies in the unit cell consistent with the recently recorded phenomenon of SnO_2 nanocrystals agglomerating to form spheres [28].

Fig. 2b shows the observed and calculated XRD patterns for cubic PbS (ICSD 62190, space group Fm-3m, $a = 5.9143$ Å). Broad signals again suggest particle size in the nanometer regime, though the peak broadening is now non-uniform and the FWHM values differ with (hkl) values. This points to the presence of anisotropy in the distribution of crystallite size and r.m.s strain. Analysis suggests that the crystallite size along the <111> direction is the smallest (~4.92 nm) and that the value of the corresponding r.m.s lattice strain is 1.39×10^{-2}, whereas particle size is largest along <200> direction with a r.m.s lattice strain value of 1.36×10^{-2}. The r.m.s lattice strain in the cubic PbS lattice in all crystallographic directions is greater than that seen above for SnO_2 [19].

Fig. 2c shows the observed and simulated XRD patterns for heterostructured SnO_2/PbS (see below for microscopic corroboration of this morphology). Data comprise reflections attributable to both tetragonal SnO_2 and cubic PbS phases with the (110), (211), (112) and (301) peaks of tetragonal SnO_2 overlapping with those of the (111), (311), (222) and (400) planes of cubic PbS. Analysis of such severely overlapping reflections necessitates use of the Rietveld whole profile fitting method [22]. Using this, the volume percentages of tetragonal SnO_2 phase and cubic PbS phase were found to be 61.42 and 38.58%, respectively. Calculated values of the lattice parameters of the core in heterostructured SnO_2/PbS are $a = 4.8937$ Å and $c = 3.0993$ Å. These values show an increase and a decrease, respectively, in relation to the corresponding values for bulk SnO_2 (ICSD 154960). These data gave unit cell volumes for SnO_2 of 75.343 Å^3 and 74.223 Å^3 in the SnO_2 NSs and heterostructured SnO_2/PbS, respectively. Both size of the primary SnO_2 nanocrystallites and r.m.s strain in the heterostructured material were calculated to be higher than those for pure SnO_2 NSs (Tables 1 and 2), and this is attributed to coverage of the core by PbS in the heterostructure [31]. In our earlier report of a homogeneous rather than a heterogeneous system [19], the most intense (200) reflection of both PbS and of nanocomposite SnO_2/PbS was perfectly simulated by considering the pV analytical function from the cubic PbS

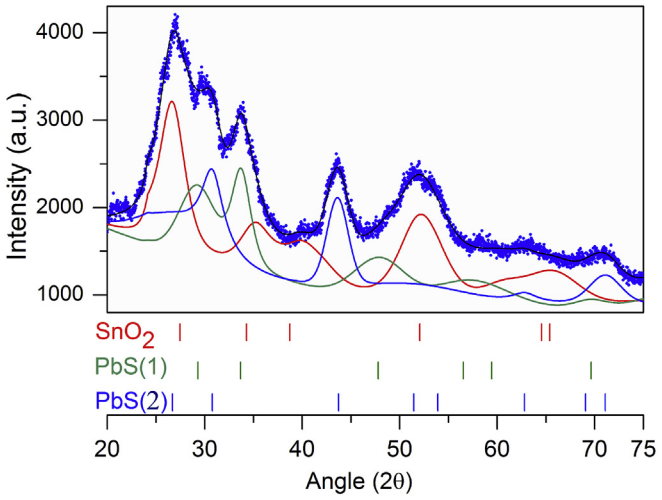

Fig. 3. The contribution of different phases (tetragonal SnO_2 and PbS(1) and PbS(2)) to the XRD pattern of heterostructured SnO_2/PbS.

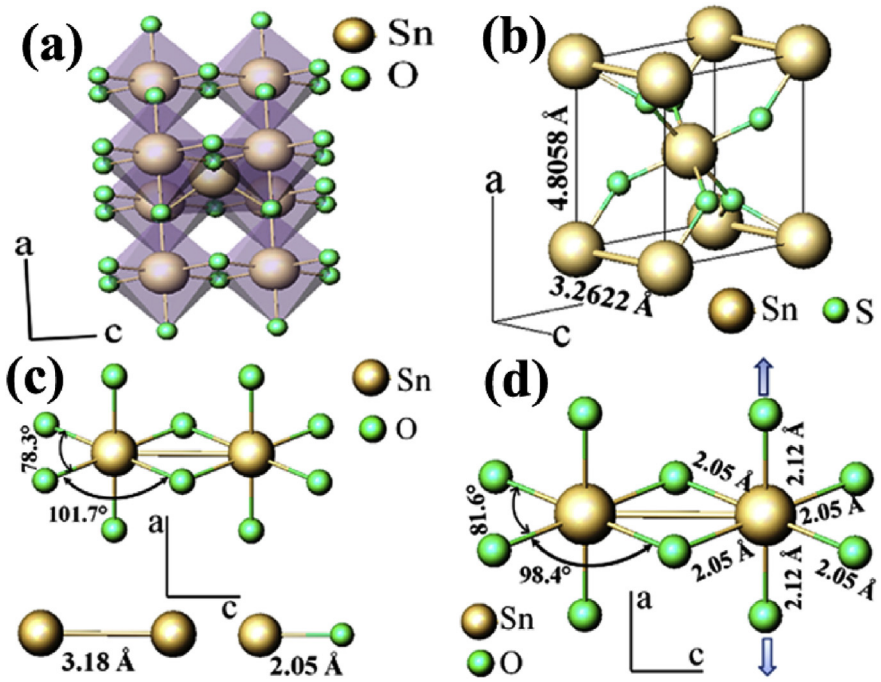

Fig. 4. Atomic arrangements in (a) the nanospherical SnO_2 crystal lattice and (b) the corresponding unit cell. Distorted SnO_6 octahedra in (c) SnO_2 NSs and (d) SnO_2/PbS heterostructures.

lattice. However, in the present case the peak shape of the (200) reflection of cubic PbS in heterostructured SnO_2/PbS differs from that of the pure PbS phase in Fig. 2b. Deconvolution (Fig. 3) suggests that this has its origins in the presence in heterostructured SnO_2/PbS of two PbS polymorphs with marginally different interplanar distances and lattice constants ($a = 5.4621$ Å and 5.9894 Å in PbS(1) and PbS(2), respectively, such that $a_{PbS(2)} > a_{PbS} > a_{PbS(1)}$). Similarly, whereas the (200) reflection is the most intense reflection in cubic PbS, its relative intensity is smaller in the heterostructured material. This is attributable to overlap of the (110) reflection of tetragonal SnO_2 with the (111) reflection of cubic PbS in heterostructured SnO_2/PbS. The ratio of volume fractions of PbS(1) and PbS(2) is found to be 3:4. Like cubic PbS in Fig. 2b, both PbS(1) and PbS(2) phases exhibit anisotropy in particle size and r.m.s lattice strain. The values of particle size and r.m.s lattice strain are again found to be maximal along the <111> direction for both PbS(1) and PbS(2) phases (Table 2).

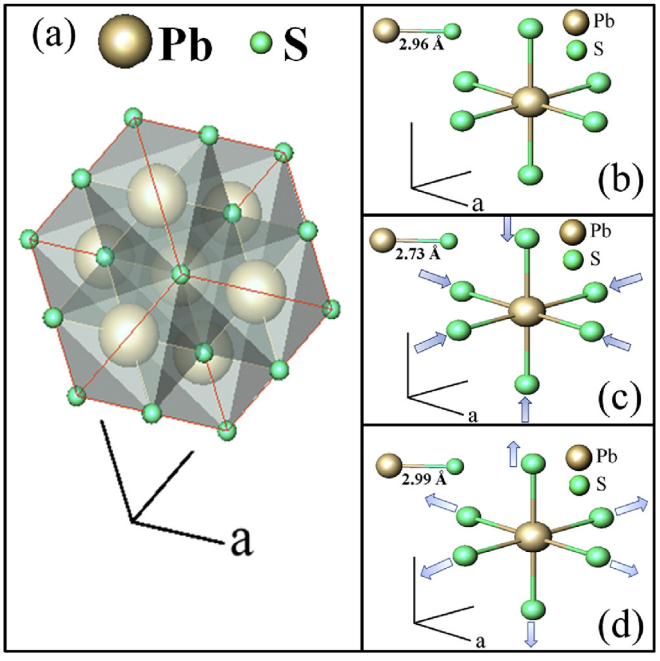

Fig. 5. (a) Unit cell of PbS NCs. Atomic arrangement of Pb and S atoms forming PbS_6 octahedra in (b) PbS NCs, and heterostructured (c) PbS(1) and (d) PbS(2).

To understand the changes in the atomic arrangement in the crystal lattice of nanospherical SnO_2 and cubic PbS in both pristine form and in heterostuctured SnO_2/PbS, the atomic modeling of tetragonal SnO_2 and cubic PbS phases was carried out. Analysis used refined structural parameters obtained from the Rietveld analysis.

3.2. Atomic modeling

To understand changes in the atomic arrangement in the crystal lattices of both pristine SnO_2 NSs and PbS NCs and in heterostuctured SnO_2/PbS, the atomic modeling of tetragonal SnO_2 and cubic PbS phases was undertaken using refined structural parameters obtained from the Rietveld analysis. The crystal structure of a SnO_2 NS is shown in Fig. 4a. The refined fractional coordinates of the atomic sites of O atoms are (0.306, 0.305, 0), with the Sn atoms occupying voids at the centres of oxygen octahedra. The tetragonal unit cell of nanospherical SnO_2 is shown in Fig. 4b while Fig. 4c shows the atomic arrangement of Sn and O atoms in more detail; Sn–O = 2.05 Å, Sn···Sn = 3.18 Å, O–Sn–O (in the equatorial plane) = 78.3° and 101.7°. These last data indicate that the octahedra formed are irregular. Similar data for the SnO_2 octahedra in heterostructured SnO_2/PbS (Fig. 4d) demonstrate equatorial Sn–O bond lengths that remain unchanged with respect to those in the uncoated SnO_2 NSs. In contrast, the axial Sn–O bonds increase from 2.05 Å to 2.12 Å along the *a*-axis. Lastly, the O–Sn–O bond angles in the equatorial plane have also changed on account of formation of

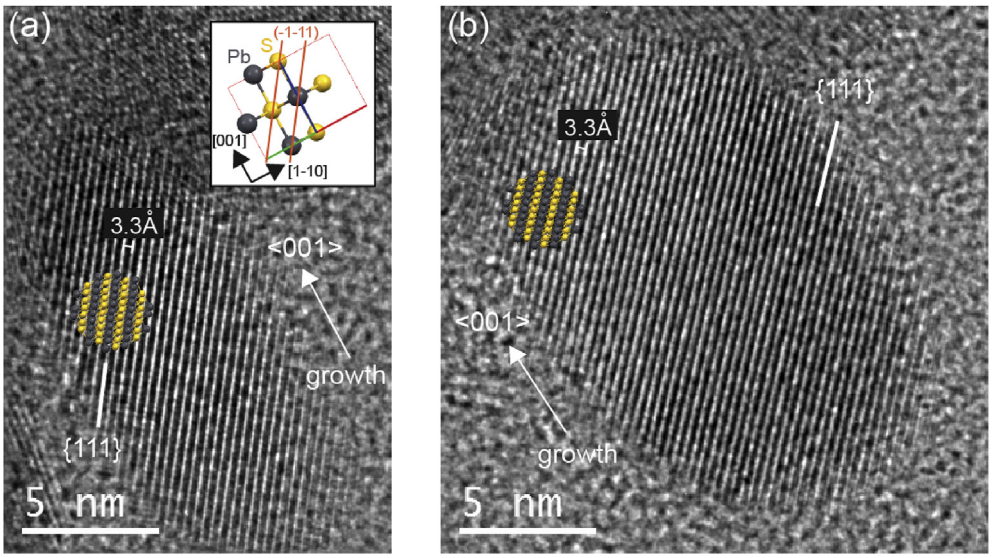

Fig. 6. HRTEM images of representative PbS NCs oriented close to their <110> zone axes. The {111} crystallographic planes are resolved in the elongated NCs imaged in both (a) and (b). The superimposed crystal model (Pb = grey, S = yellow), tilted slightly from the <110> zone axis, displays the orientation relationship between the unit cell (insert) and the image. (For interpretation of the references to colour in this figure legend, the reader is referred to the web version of this article.)

the heterostructure.

The cubic PbS unit cell is shown in Fig. 5a. The atomic coordinates of Pb and S atoms in the PbS_6 octahedra are (0.5, 0.5, 0.5) and (0, 0, 0), respectively. These octahedra in the cube-shaped PbS nanostructure reveal Pb–S = 2.96 Å (Fig. 5b). Moving to SnO_2/PbS, the Pb–S bonds in PbS(1) decrease to 2.73 Å, resulting in a decreased *a*. The reverse phenomenon is observed in PbS(2), with the Pb–S bonds expanding equally to 2.99 Å to increase *a*.

3.3. TEM analysis

HRTEM images of selected elongated PbS NCs are shown in Fig. 6. The inter-planar spacing of the resolved lattice fringes in the representative NCs shown was measured to be 3.3 ± 0.2 Å. This spacing is within experimental error of that expected for the {111} crystallographic planes of PbS (3.41 Å). Assuming the long axes of the NCs lie in the imaging plane, the particles are imaged close to their <110> zone axes and the growth of both NCs has occurred in the <001> direction, this assignment is in excellent agreement with the XRD analysis reported above. Fig. 7a–d shows representative TEM images of SnO_2 NSs (a/b) and SnO_2/PbS heterostructures (c/d). Fig. 7a confirms the formation of a narrow SnO_2 NS size distribution with a mean sphere diameter of approximately 180 nm (Fig. 7b). Fig. 7c corroborates the deposition of PbS NCs on the surface of the preformed SnO_2 NSs to yield heterostructures typically 250 nm in diameter (Fig. 7d). While Fig. 7c/d indicate near complete uptake of PbS by the SnO_2 NSs, a low level of remnant isolated PbS NCs can be seen. Interestingly, a survey of particle sizes reveals a bimodal distribution. The isolated PbS NCs in Fig. 7c reveal a monocrystalline habit and a MPS of 24.0 ± 2.5 nm (Fig. 7e), which corresponds with the MPS previously documented in the Sn-free synthesis of pure PbS nanocubes using $Na_2S{\cdot}9H_2O$ and $Pb(NO_3)_2$ [19]. In contrast, PbS NCs that are attached to SnO_2 NSs appear significantly larger, demonstrating a MPS which, at 39.5 ± 2.0 nm (Fig. 7f), reinforces the Rietveld analysis of PbS phase(s) in heterostructured SnO_2/PbS (Table 2). This TEM analysis of either type of PbS NC suggests that in this system PbS NC formation can occur independently of coexisting SnO_2 NSs. The observation of larger PbS NCs coating the NSs is consistent with the limited agglomeration of nanocrystalline PbS NCs at the SnO_2 NS surface, though the formation of a bimodal distribution of monocrystalline PbS NCs of which the larger show a greater tendency for nucleation or deposition on SnO_2 cannot be ruled out. Additional TEM data for heterostructured SnO_2/PbS is provided in ESI Figure S1.

Fig. 8a and b displays HAADF-STEM images of representative heterostructure clusters in which aggregates of small NCs appear to decorate the surface of larger spherical particles to varying degrees. The so called 'Z-contrast' inherent to the HAADF-STEM imaging technique suggests that the NCs and larger spherical particles are uniform in composition. EDX analysis reinforces this view by confirming the presence of lead and sulfur in the smaller NCs (Fig. 8c). Carbon, oxygen, silicon and copper X-rays are also detected but likely arise from the thin amorphous carbon membrane, a thin oxide layer, internal fluorescence in the silicon detector and the copper grid bars of the sample grid, respectively. The EDX spectrum obtained from a large spherical particle confirms the presence of tin and oxygen. Lead and sulfur X-rays are also detected from decorating PbS nanoparticles in addition to the extraneous X-rays aforementioned. Elemental mapping data from the HAADF-STEM image of a SnO_2/PbS heterostructure is provided in ESI Figure S2.

3.4. Raman spectroscopy

Fig. 9a shows the room temperature Raman spectrum of SnO_2 NSs. The shoulder at 486 cm^{-1} corresponds to the E_g mode and is consistent with rutile bulk SnO_2. Meanwhile, the 573 cm^{-1} absorption is a surface defect mode [32] mostly due to surface oxygen vacancies [33]. It is large compared to the E_g mode and this is consistent with the large surface area of the small primary nanocrystallites identified as comprising the sphere (see above). Fig. 9b shows the Raman spectrum of heterostructured SnO_2/PbS. It contains bands at 429 cm^{-1}, 602 cm^{-1} and 967 cm^{-1}. These are attributable to 2LO, 3LO and the laser-induced degradation of PbS (see ref. 19 for data on PbS). Notably, the 573 cm^{-1} SnO_2 surface defect mode is no longer present, consistent with modification of the SnO_2 NS surface by PbS.

3.5. XPS analysis

Fig. 10a shows peaks at 485.7 and 494.1 eV corresponding to

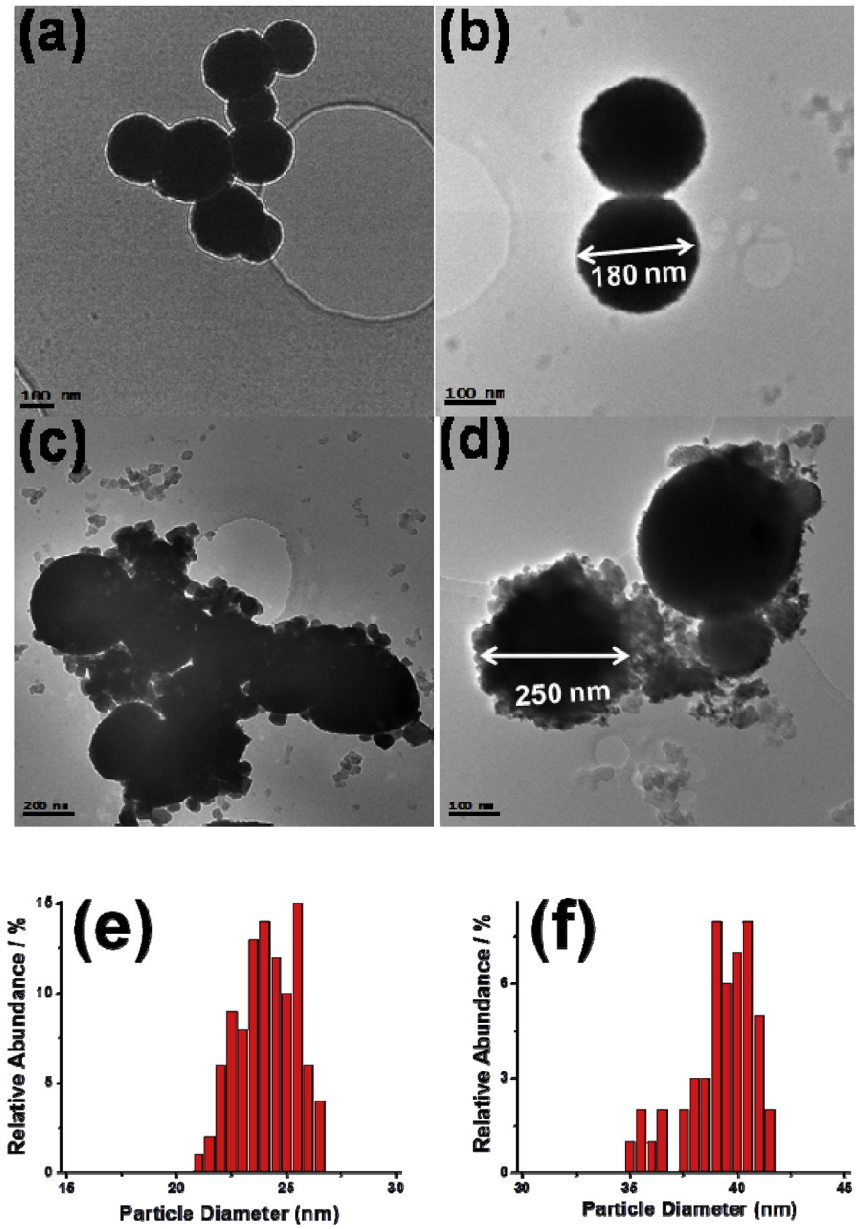

Fig. 7. Representative TEM images of SnO_2 NSs (a, b) and SnO_2/PbS heterostructures (c, d). Scale bars 100 nm (a, b, d) and 200 nm (c). Size distribution analysis for isolated (e) and NS-coating (f) PbS NCs (100 particles of each) seen in (c).

$Sn3d_{5/2}$ and $Sn3d_{3/2}$, respectively [34]. These are attributable to Sn(IV) (indexed Standard ESCA Spectra of the Elements and Line Energy Information, ϕCo., USA) [35] and are consistent with SnO_2 [36]. The characteristic O1s peak at 529.6 eV (Fig. 10b) is attributed to the lattice oxygen in SnO_2. XPS data for heterostructured SnO_2/PbS are shown in Fig. 11. Fig. 11a demonstrates the high resolution spectrum for the Sn3d region and reveals symmetric signals attributable to the $Sn3d_{5/2}$ and $Sn3d_{3/2}$ binding energies of Sn(IV). An O1s peak is observed at 530.0 eV (Fig. 11b), while peaks at 137.6 eV and 142.4 eV are attributable to $Pb4f_{7/2}$ and $Pb4f_{5/2}$, respectively (Fig. 11c). Lastly, S2p is characterized by peaks at 161.6 eV and 159.4 eV alongside a S(VI) peak at 167.5 eV (Fig. 11d). Taken together with XRD and TEM results, XPS data point to the SnO_2/PbS heterostructures being composed of Sn(IV), Pb(II), O, and S. Recent work revealed that the $Pb4f_{7/2}$ and $Pb4f_{5/2}$ peaks due to nanoscopic PbS showed high energy shoulders consistent with limited PbO formation [19]. The corresponding signals in heterostructured SnO_2/PbS reside predominantly at the high-energy positions, with the presence of low energy shoulders now signifying that heterostructure formation results in a greater proportion of Pb residing in close proximity to O [37]. This behaviour differs again from that seen in homogeneous SnO_2/PbS nanocomposites, in which Pb-based regions were essentially amorphous and Pb signals had completely migrated to the high energy positions [19].

3.6. UV–vis spectroscopy

Consistent with previous work [38], Fig. 12a shows absorption edges at 289 and 221 nm for ethanolic SnO_2 NSs. Meanwhile the spectrum of pure PbS NCs has been reported to reveal absorption edges at 362 nm and 278 nm [19]. The UV–Vis absorption spectrum of heterostructured SnO_2/PbS (Fig. 12b) exhibits two absorption bands; 224 nm (assigned to SnO_2) [39] and 267 nm

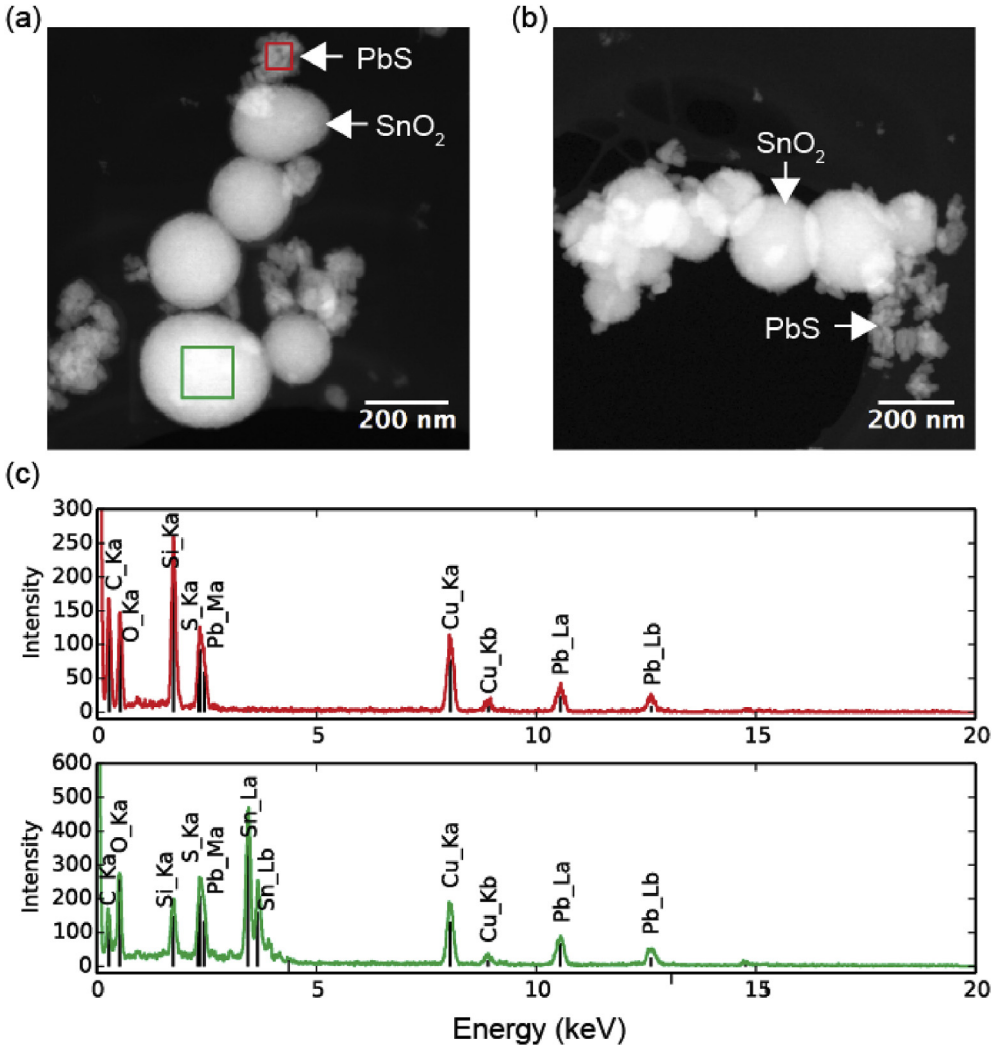

Fig. 8. (a,b) Representative HAADF-STEM images of SnO_2/PbS heterostructure clusters. (c) EDX spectra obtained from a region enclosing (red) PbS NCs and (green) a SnO_2 NS decorated by PbS NCs. Spurious copper X-rays originating from the supporting copper grid are also detected. (For interpretation of the references to colour in this figure legend, the reader is referred to the web version of this article.)

(assigned to PbS) [40].

3.7. *Photocatalytic activity tests*

Photocatalytic activity was measured in triplicate for the reaction of each catalyst (5.0 mg) with 25 ml of 1.0×10^{-5} M aqueous RhB under simulated solar irradiation. Fig. 13 shows RhB $\lambda_{max} = 555$ nm as a function of time, with the decrease in λ_{max} clearly greatest for the use of heterostructured photocatalyst. Fig. 14a shows the decomposition rate for RhB in each test, C_0 and C being the concentrations of RhB before and after irradiation, respectively. Remarkably, 81.6 (±0.8) % of the dye was degraded by the presence of SnO_2/PbS heterostructures after 300 min irradiation, whereas only 44.3 (±3.9) % and 43.1 (±4.4) % degradation was observed for the use of pure SnO_2 NSs and PbS NCs, respectively. Reaction rate constants (k) were calculated assuming pseudo first-order kinetics (Eqn. (3)) for a low initial pollutant concentration [41]:

$$\ln(C_0/C) = kt \quad (3)$$

Fig. 14b confirms first order kinetics, with $k = 1.8 \times 10^{-3}$

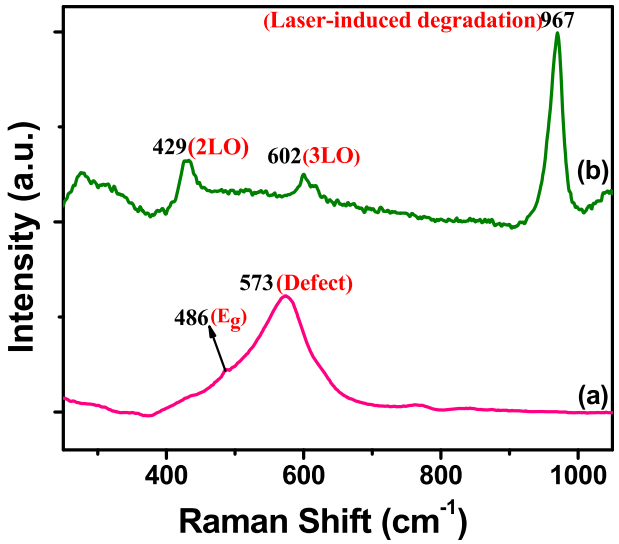

Fig. 9. Raman spectra of (a) SnO_2 NSs and (b) SnO_2/PbS heterostructures. For PbS data see Ref. [19].

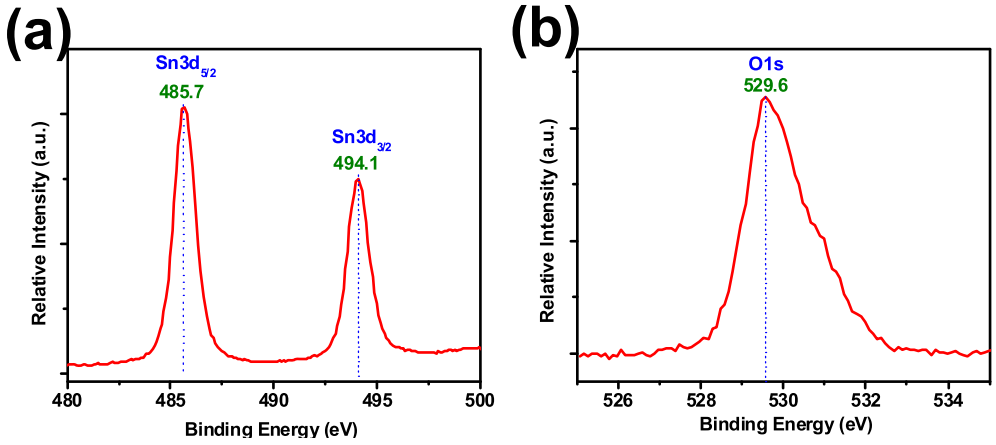

Fig. 10. XPS data for SnO_2 NSs. Binding energy spectra for (a) Sn3d; (b) O1s. For data on PbS NCs see Ref. [19].

$(\pm 0.2 \times 10^{-3})$, 1.4×10^{-3} $(\pm 0.1 \times 10^{-3})$ and 4.6×10^{-3} $(\pm 0.2 \times 10^{-3})$ min^{-1} for SnO_2 NSs, PbS NCs and SnO_2/PbS heterostructures, respectively. For the photodegradation of aqueous RhB by heterostructured SnO_2/PbS, φ_x was determined to be 0.0469 (±0.0019) mol min^{-1} W^{-1}.

The stability of the photocatalytic performance of the SnO_2/PbS heterostructured catalyst was evaluated since this is an important factor in practical applications. Catalyst cycling experiments were undertaken with the catalyst recovered by centrifugation between tests. Fig. 15a suggests that after three RhB photodegradation cycles the activity of SnO_2/PbS heterostructures had undergone some loss of activity; the efficiency of the catalyst being 81.6, 64.1, and 49.1% in the first, second, and third tests, respectively. The decrease in activity could be assigned to washout loss of some catalyst during the recovery steps. We also consider that the reduced effectiveness of the catalyst after recycling is contributed to by photobleaching of the catalyst surface [42]. The crystalline structure of the SnO_2/PbS heterostructured catalyst has been investigated after photodegradation experiments. Fig. 15b illustrates the XRD patterns of photocatalysts before and after three RhB decomposition cycles, with the lack of observable changes indicating that both crystalline phase and structure remain intact.

Semiconductor photocatalysts absorb sunlight when the energy of the incident photons is equal to or larger than the band gap of the semiconductor [43]. Thus, an electron is excited from the valence band (VB) of the semiconductor into its conduction band (CB) [44].

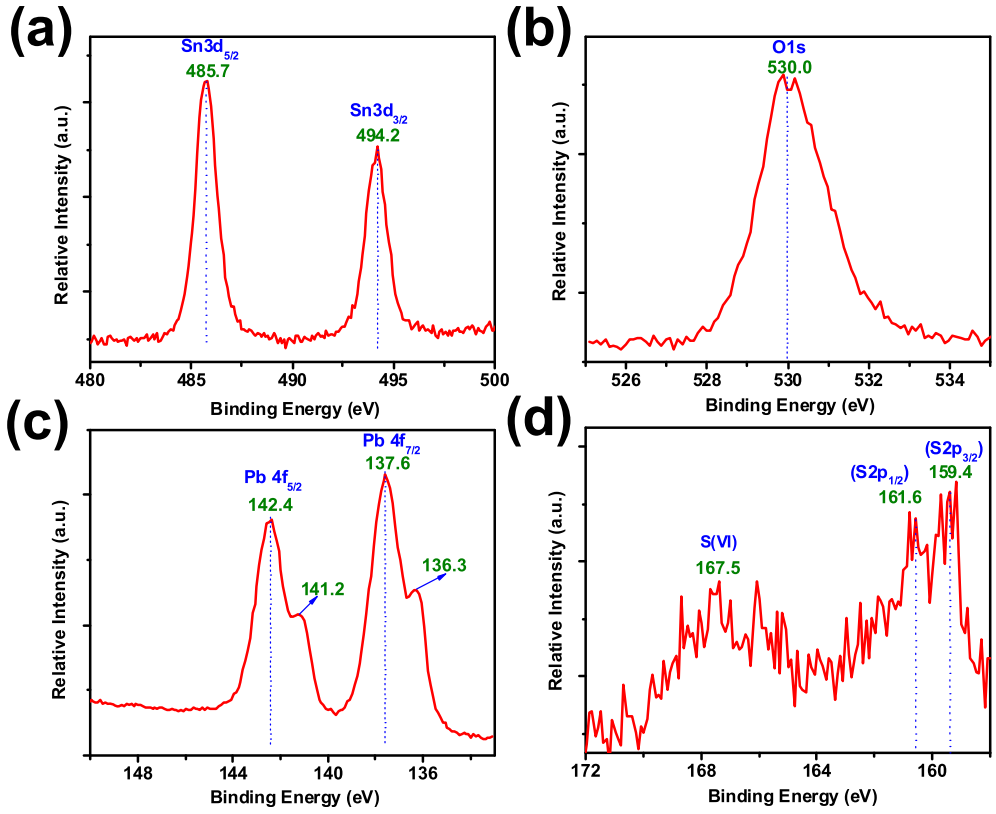

Fig. 11. XPS data for SnO_2/PbS heterostructures: binding energy spectra for (a) Sn3d; (b) O1s; (c) Pb4f; (d) S2p.

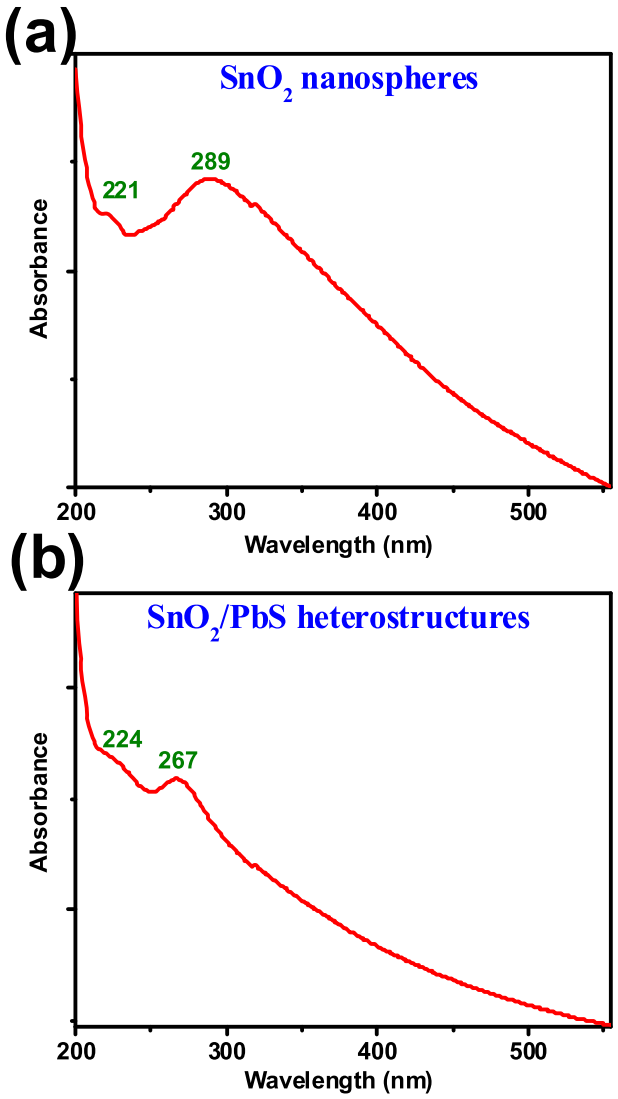

Fig. 12. UV–Vis absorption spectra of (a) SnO_2 NSs and (b) SnO_2/PbS heterostructures in ethanol. For PbS data see Ref. [19].

The photoexcited electron can be used to carry out electrochemical reduction reactions at the photocatalyst surface whereas the photoexcited hole can execute electrochemical oxidation of compounds with oxidation potentials more negative than that of the VB maximum [45]. To enable the photolytic creation of active hydroxyl radicals (OH•), the VB and the CB of the semiconductor photocatalyst should encapsulate both the oxidation potential of OH• and the reduction potential of superoxide radicals (O_2^{-}•) [46]. According to recent work [19], neither SnO_2 nor PbS independently meet the thermodynamic requirements for OH• generation. However, heterostructured SnO_2/PbS is postulated to be capable of both the separation and transportation of photoinduced charge carriers. Fig. 16 illustrates how this heterostructure reduces the electron-hole recombination probability through the migration of photogenerated electrons from the CB of PbS to that of SnO_2 at the same time as the photogenerated holes in the VB of SnO_2 move into that of PbS. Electron acceptors such as adsorbed O_2 can easily trap electrons at the SnO_2 surface to produce superoxide radical anions, which undergo protonation to produce hydroperoxy radicals (HO_2•). In water, these then give OH•, which is strongly oxidizing and can decompose RhB [47]. Finally, the photoinduced holes in PbS can also be trapped by OH^{-}, so acting as an additional OH• source.

Overall, the mechanism by which RhB undergoes photocatalytic degradation can be summarized as:

$$PbS + h\nu \rightarrow PbS\,(e^{-}_{CB} + h^{+}_{VB})$$

$$PbS\,(e^{-}_{CB}) + SnO_2 \rightarrow SnO_2\,(e^{-}_{CB}) + PbS$$

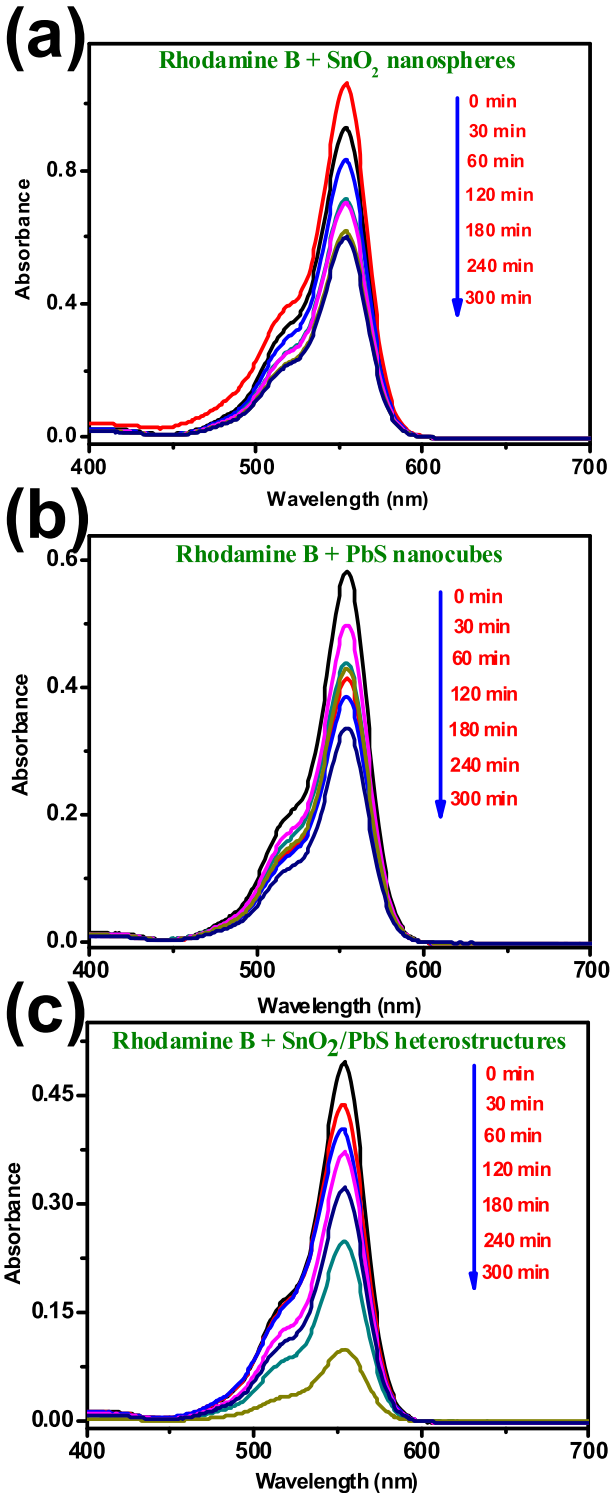

Fig. 13. Photolytically-induced changes to the RhB absorption maximum at *ca.* 555 nm catalyzed by (a) SnO_2 NSs, (b) PbS NCs and (c) SnO_2/PbS heterostructures.

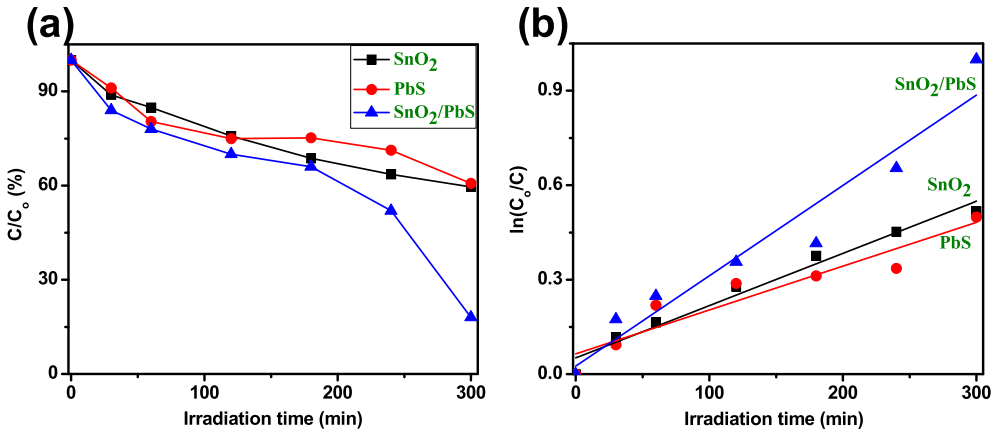

Fig. 14. (a) Plot of C/C_0 (%) (where C_0 and C are the concentrations of dye before and after irradiation, respectively) for RhB as a function of irradiation time in the presence of SnO_2 NSs, PbS NCs and SnO_2/PbS heterostructures. (b) Plot of $\ln(C_0/C)$ as a function of irradiation time.

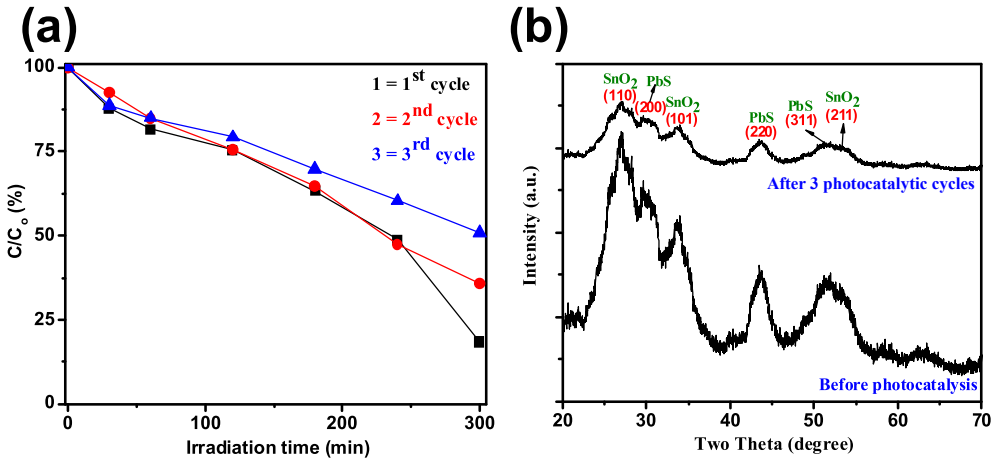

Fig. 15. (a) Recyclability of heterostructured SnO_2/PbS and (b) XRD patterns of the catalyst before and after three cycles of RhB photodecomposition.

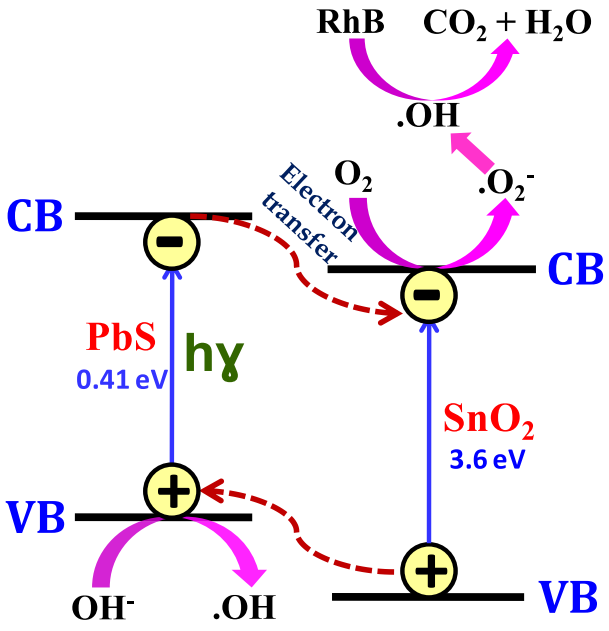

Fig. 16. Proposed model for the photocatalytic activity of SnO_2/PbS heterostructures.

$$SnO_2\ (e^-_{CB}) + O_2 \rightarrow SnO_2 + O_2^{-\bullet}$$

$$O_2^{-\bullet} + H_2O \rightarrow HO_2^{\bullet} + OH^-$$

$$HO_2^{\bullet} + H_2O \rightarrow OH^{\bullet} + H_2O_2$$

$$H_2O_2 \rightarrow 2OH^{\bullet}$$

$$PbS\ (h^+_{VB}) + OH^- \rightarrow OH^{\bullet} + PbS$$

$$OH^{\bullet} + RhB \rightarrow CO_2 + H_2O$$

To verify that the photocatalytic degradation pathway afforded by the current heterostructured SnO_2/PbS system proceeds via photoinduced $OH^{\bullet}$ radical creation, a TA probe was employed whereby reaction with $OH^{\bullet}$ radicals gave fluorescent TAOH [48]. Upon excitation at 315 nm, the highest intensity at 425 nm progressively increased with irradiation time (Fig. 17), demonstrating $OH^{\bullet}$ photogeneration.

3.8. BET surface area analysis

BET surface areas and pore size distributions of the SnO_2 NSs and SnO_2/PbS heterostructures were determined by measuring nitrogen adsorption-desorption isotherms (Fig. 18). Samples exhibited

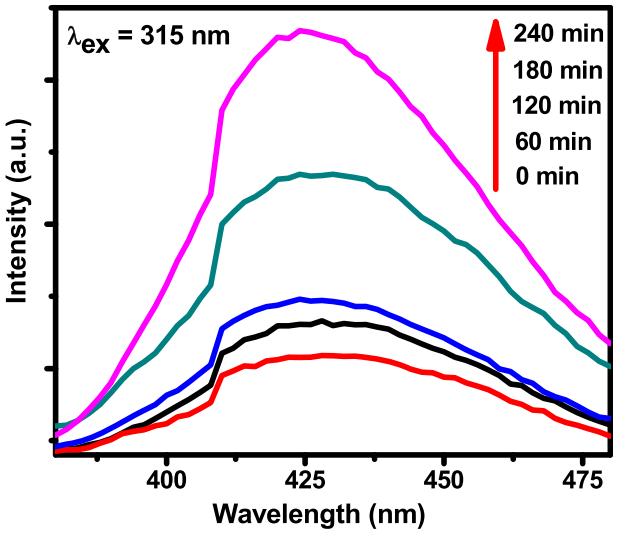

Fig. 17. Fluorescence spectral changes measured during illumination of heterostructured SnO_2/PbS in a basic TA solution (excitation at 315 nm).

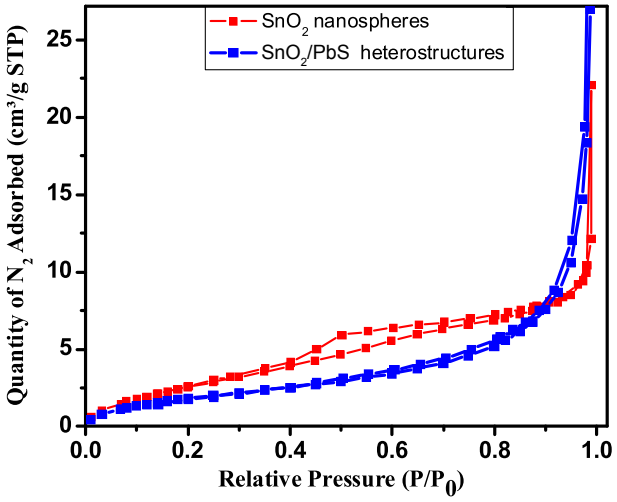

Fig. 18. Nitrogen adsorption-desorption isotherms at 77 K (P and P_0 are the equilibrium and the saturation pressures of N_2 at the temperature of adsorption) for SnO_2 NSs and SnO_2/PbS heterostructures.

type IV behaviour and distinct H2-type hysteresis loops [49], suggesting an interconnected network of mesopores. Pore size distributions were determined by applying Barrett-Joyner-Halenda (BJH) analysis to the adsorption branch of each isotherm (Table 3). Interestingly, results showed that the SnO_2/PbS heterostructures exhibit a lower surface area than either SnO_2 NSs (Table 3) or PbS NCs. This points to the importance of the type-II electronic structure in defining the superior photocatalytic activity of the heterostructure.

Table 3
Nitrogen sorption porosimetry studies[a] of SnO_2 NSs and SnO_2/PbS heterostructures. For PbS NC data see Ref. [19].

Photocatalyst	S_{BET} ($m^2\ g^{-1}$)	Pore volume ($cm^3\ g^{-1}$)	Mean pore size (nm)
SnO_2	10.0698	0.034046	10.8651
SnO_2/PbS	7.1488	0.157042	69.4260

[a] Surface areas determined by the BET technique, mean pore diameters by BJH theory (applied to the adsorption branch), and pore volumes by single-point analysis.

4. Conclusions

In summary, we have developed a simple and inexpensive approach to the controlled synthesis of a heterostructured SnO_2 NS/PbS NC photocatalyst. Its structure has been unambiguously demonstrated by an exhaustive combination of XRD, TEM, BET, XPS and Raman spectral studies. Detailed Rietveld analysis has established the occurrence of both cubic and tetragonal phases in the heterostructure and (micro)structural parameters have been elucidated. The heterostructured material demonstrated superior photocatalytic activity in the degradation of RhB under simulated solar irradiation when compared to either SnO_2 or PbS. In the light of BET surface area measurements, effective electron-hole separation at the interface of the two semiconductors is believed to be mainly responsible for this enhanced performance. In turn, this idea of the facile production of heterojunction-containing semiconducting photocatalysts with elevated activity suggests a pioneering approach to catalyst design and fabrication that addresses environmental concerns. That said, it is clear that the performance of heterostructured SnO_2/PbS currently shows some subsidence when the catalyst is recycled. This may be attributable to incomplete catalyst recovery. The further development of heterostructured SnO_2/PbS as a potential photocatalyst will therefore focus on immobilization studies. The development of novel matrices that offer new possibilities in this respect is now being initiated.

Acknowledgements

A. K. acknowledges support from the Royal Society's Newton International Fellowship scheme (NF130808). B. R. K. thanks the UK EPSRC for financial support (EP/J500380/1). Thanks go also to Drs. Tim Jones and Jill Geddes of Schlumberger Gould Research for help with the acquisition of Raman and X-ray photoelectron spectra, to Dr. Zlatko Saracevic of the Department of Chemical Engineering and Biotechnology (University of Cambridge) for help with BET surface area analysis, and to Mr. Tom Jellicoe for help with the photoluminescence measurements. Open Data for this paper are available at the University of Cambridge data repository (https://doi.org/10.17863/CAM.6905).

Appendix A. Supplementary data

Supplementary data related to this article can be found at http://dx.doi.org/10.1016/j.jallcom.2016.12.167.

References

[1] (a) Y. Anjaneyulu, N.S. Chary, D.S.S. Raj, Decolourization of industrial effluents-available methods and emerging technologies - a review, Rev. Environ. Sci. Biotechnol. 4 (2005) 245–273;
(b) S.P. Buthelezi, A.O. Olaniran, B. Pillay, Textile dye removal from wastewater effluents using bioflocculants produced by indigenous bacterial isolates, Molecules 17 (2012) 14260–14274;
(c) A.E. Ghaly, R. Ananthashankar, M. Alhattab, V.V. Ramakrishnan, Production, characterization and treatment of textile effluents: a critical review, J. Chem. Eng. Process Technol. 5 (2014) 1000182, 19 pages.
[2] (a) M. Neumann, K. Zeitler, Application of microflow conditions to visible light photoredox catalysis, Org. Lett. 14 (2012) 2658–2661;
(b) T. Noël, X. Wang, V. Hessel, Accelerating photoredox catalysis in continuous microflow, Chim. Oggi 31 (2013) 10–14;
(c) N.J.W. Straathof, D.J.G.P. van Osch, A. Schouten, X. Wang, J.C. Schouten, V. Hessel, T. Noël, Visible light photocatalytic metal-free perfluoroalkylation of heteroarenes in continuous flow, J. Flow. Chem. 4 (2014) 12–17;
(d) Y. Su, A. Talla, V. Hessel, T. Noël, Controlled photocatalytic aerobic oxidation of thiols to disulfides in an energy efficient photomicroreactor,

Chem. Eng. Technol. 38 (2015) 1733–1742;
(e) A. Talla, B. Driessen, N.J.W. Straathof, L.G. Milroy, L. Brunsveld, V. Hessel, T. Noël, Metal-free photocatalytic aerobic oxidation of thiols to disulfides in batch and continuous-flow, Adv. Synth. Catal. 357 (2015) 2180–2186.
[3] S. Rubio, D. Perez-Bendito, Recent advances in environmental analysis, Anal. Chem. 81 (2009) 4601–4622.
[4] M.R. Hoffmann, S.T. Martin, W. Choi, D.W. Bahnemannt, Environmental applications of semiconductor photocatalysis, Chem. Rev. 95 (1995) 69–96.
[5] (a) C. Wang, C. Shao, Y. Liu, X. Li, Water-dichloromethane interface controlled synthesis of hierarchical rutile TiO_2 superstructures and their photocatalytic properties, Inorg. Chem. 48 (2009) 1105–1113;
(b) C. Ye, Y. Bando, G. Shen, D. Golberg, Thickness-dependent photocatalytic performance of ZnO nanoplatelets, J. Phys. Chem. B 110 (2006) 15146–15151;
(c) L. Li, Y. Chu, Y. Liu, L. Dong, Template-free synthesis and photocatalytic properties of novel Fe_2O_3 hollow spheres, J. Phys. Chem. C 111 (2007) 2123–2127.
[6] C. Wang, C. Shao, X. Zhang, Y. Liu, SnO_2 nanostructures-TiO_2 nanofibers heterostructures: controlled fabrication and high photocatalytic properties, Inorg. Chem. 48 (2009) 7261–7268.
[7] (a) K.Y. Song, M.K. Park, Y.T. Kwon, H.W. Lee, W.J. Chung, W.I. Lee, Preparation of transparent particulate MoO_3/TiO_2 and WO3/TiO_2 films and their photocatalytic properties, Chem. Mater. 13 (2001) 2349–2355;
(b) R. Ostermann, D. Li, Y. Yin, J.T. McCann, Y. Xia, V_2O_5 nanorods on TiO_2 nanofibers: a new class of hierarchical nanostructures enabled by electrospinning and calcination, Nano Lett. 6 (2006) 1297–1302;
(c) G. Marci, V. Augugliaro, M.J. Lopez-Munoz, C. Martin, L. Palmisano, V. Rives, M. Schiavello, R.J.D. Tilley, A.M. Venezia, Preparation, characterization and photocatalytic activity of polycrystalline ZnO/TiO_2 systems. 2. Surface, bulk characterization, and 4-nitrophenol photodegradation in liquid-solid regime, J. Phys. Chem. B 105 (2001) 1033–1040;
(d) S. Mathur, S. Barth, Molecule-based chemical vapor growth of aligned SnO_2 nanowires and branched SnO_2/V_2O_5 heterostructures, Small 3 (2007) 2070–2075.
[8] B. Liu, X. Zhao, N. Zhang, Q. Zhao, X. He, J. Feng, Photocatalytic mechanism of TiO_2-CeO_2 films prepared by magnetron sputtering under UV and visible light, Surf. Sci. 595 (2005) 203–211.
[9] L. Zheng, Y. Zheng, C. Chen, Y. Zhan, X. Lin, Q. Zheng, K. Wei, J. Zhu, Network structured SnO_2/ZnO heterojunction nanocatalyst with high photocatalytic activity, Inorg. Chem. 48 (2009) 1819–1825.
[10] Z. Zhang, C. Shao, X. Li, L. Zhang, H. Xue, C. Wang, Y. Liu, Electrospun nanofibers of ZnO-SnO_2 heterojunction with high photocatalytic activity, J. Phys. Chem. C 114 (2010) 7920–7925.
[11] W. Wu, S.F. Zhang, X.H. Xiao, J. Zhou, F. Ren, L.L. Sun, C.Z. Jiang, Controllable synthesis, magnetic properties, and enhanced photocatalytic activity of spindle like mesoporous α-Fe_2O_3/ZnO core-shell heterostructures, ACS Appl. Mater. Interfaces 4 (2012) 3602–3609.
[12] M. Niu, F. Huang, L. Cui, P. Huang, Y. Yu, Y. Wang, Hydrothermal synthesis, structural characteristics, and enhanced photocatalysis of SnO_2/α-Fe_2O_3 semiconductor nanoheterostructures, ACS Nano 4 (2010) 681–688.
[13] J.C. Kim, J. Choi, Y.B. Lee, J.H. Hong, J.I. Lee, J.W. Yang, W.I. Lee, N.H. Hur, Enhanced photocatalytic activity in composites of TiO_2 nanotubes and CdS nanoparticles, Chem. Commun. (2006) 5024–5026.
[14] P. Kundu, P.A. Deshpande, G. Madras, N. Ravishankar, Nanoscale ZnO/CdS heterostructures with engineered interfaces for high photocatalytic activity under solar radiation, J. Mater. Chem. 21 (2011) 4209–4216.
[15] A. Kar, S. Kundu, A. Patra, Photocatalytic properties of semiconductor SnO_2/CdS heterostructure nanocrystals, RSC Adv. 2 (2012) 10222–10230.
[16] Z. Liu, D.D. Sun, P. Guo, J.O. Leckie, An efficient bicomponent TiO_2/SnO_2 nanofiber photocatalyst fabricated by electrospinning with a side-by-side dual spinneret method, Nano Lett. 7 (2007) 1081–1085.
[17] T. Gao, T. Wang, Sonochemical synthesis of SnO_2 nanobelt/CdS nanoparticle core/shell heterostructures, Chem. Commun. (2004) 2558–2559.
[18] P. Ghosh, A. Kar, A. Patra, Structural and photoluminescence properties of doped and core-shell $LaPO_4$: Eu^{3+} nanocrystals, J. Appl. Phys. 108 (2010) 113506, 1–8.
[19] A. Kar, S. Sain, D. Rossouw, B.R. Knappett, S.K. Pradhan, A.E.H. Wheatley, Facile synthesis of SnO_2-PbS nanocomposites with controlled structure for applications in photocatalysis, Nanoscale 8 (2016) 2727–2739.
[20] A. Kar, A. Datta, A. Patra, Fabrication and optical properties of core/shell CdS/$LaPO_4$:Eu nanorods, J. Mater. Chem. 20 (2010) 916–922.
[21] T. Gao, T. Wang, Sonochemical synthesis of SnO_2 nanobelt/CdS nanoparticle core/shell heterostructures, Chem. Commun. (2004) 2558–2559.
[22] (a) H.M. Rietveld, Line profiles of neutron powder-diffraction peaks for structure refinement, Acta Cryst. 22 (1967) 151–152;
(b) H.M. Rietveld, A profile refinement method for nuclear and magnetic structures,, J. Appl. Cryst. 2 (1969) 65–71;
(c) R.A. Young, D.B. Willes, Profile shape functions in Rietveld refinements, J. Appl. Cryst. 15 (1982) 430–438.
[23] (a) L. Lutterotti The Maud Program, http://maud.radiographema.com/. (b) L. Lutterotti, Total pattern fitting for the combined size-strain-stress-texture determination in thin film diffraction, Nucl. Instr. Method. Phys. Res. B 268 (2010) 334–340.
[24] (a) P. Scardi, L. Lutterotti, A. Tomasi, XRD characterization of multilayered systems, Thin Solid Films 236 (1993) 130–134;
(b) R.A. Young, The Rietveld Method, International Union of Crystallography, Oxford University Press, New York, 1996.
[25] S. Sain, S. Patra, S.K. Pradhan, Microstructure and optical band-gap of mechanosynthesized $Cd_xZn_{1-x}S$ quantum dots, J. Phys. D. Appl. Phys. 44 (2011) 075101, 8 pp.
[26] L. Lutterotti, P. Scardi, Simultaneous structure and size-strain refinement by the Rietveld method, J. Appl. Cryst. 23 (1990) 246–252.
[27] S. Sain, S.K. Pradhan, Mechanochemical solid state synthesis of $(Cd_{0.8}Zn_{0.2})S$ quantum dots: microstructure and optical characterizations, J. Alloy Compd. 509 (2011) 4176–4184.
[28] S. Sain, A. Kar, A. Patra, S.K. Pradhan, Structural interpretation of SnO_2 nanocrystals of different morphologies synthesized by microwave irradiation and hydrothermal methods, CrystEngcomm 16 (2014) 1079–1090.
[29] Y. Xu, C.H. Langford, UV- or visible-light-induced degradation of X3B on TiO_2 nanoparticles: the influence of adsorption, Langmuir 17 (2001) 897–902.
[30] J.M. Buriak, P.V. Kamat, K.S. Schanze, Best practices for reporting on heterogeneous photocatalysis, ACS Appl. Mater. Interfaces 6 (2014) 11815–11816.
[31] S. Sain, A. Kar, A. Patra, S.K. Pradhan, Microstructure and photoluminescence properties of ternary $Cd_{0.2}Zn_{0.8}S$ quantum dots synthesized by mechanical alloying, J. Nanopart. Res. 16 (2014) 2673–2688.
[32] A. Kar, S. Kundu, A. Patra, Surface defect related luminescence properties of SnO_2 nanorods and nanoparticles, J. Phys. Chem. C 115 (2011) 118–124.
[33] F. Gu, S.F. Wang, M.K. Lu, G.J. Zhou, D. Xu, D.R. Yuan, Photoluminescence properties of SnO_2 nanoparticles synthesized by sol-gel method, J. Phys. Chem. B 108 (2004) 8119–8123.
[34] L. Cao, H. Wan, L. Huo, S. Hi, A novel method for preparing ordered SnO_2/TiO_2 alternate nanoparticulate films, J. Colloid Interface Sci. 244 (2001) 97–101.
[35] Y.D. Wang, C.L. Ma, X.D. Sun, H.D. Li, Preparation and characterization of SnO_2 nanoparticles with a surfactant-mediated method, Nanotechnol 13 (2002) 565–569.
[36] D. Chen, L. Gao, Novel synthesis of well-dispersed crystalline SnO_2 nanoparticles by water-in-oil microemulsion-assisted hydrothermal process, J. Colloid Interface Sci. 279 (2004) 137–142.
[37] H. Yang, X. Zhang, A. Tang, Mechanosynthesis and gas-sensing properties of In_2O_3/SnO_2 nanocomposites, Nanotechnol. 17 (2006) 2860–2864.
[38] J. Kang, S. Tsunekawa, A. Kasuya, Ultraviolet absorption spectra of amphoteric SnO_2 nanocrystallites, Appl. Surf. Sci. 174 (2001) 306–309.
[39] S.Y. Chen, H.D. Tsai, W.T. Chuang, J.J. Lee, C.Y. Tang, C.Y. Lin, S. Cheng, Direct preparation of thermally stable Sn-incorporated SBA-15 mesoporous materials in the self-generated acidic environment, J. Phys. Chem. C 113 (2009) 15226–15238.
[40] A.H. Souici, N. Keghouche, J.A. Delaire, H. Remita, A. Etcheberry, M. Mostafavi, Structural and optical properties of PbS nanoparticles synthesized by the radiolytic method, J. Phys. Chem. C 113 (2009) 8050–8057.
[41] Y. Feng, L. Li, M. Ge, C. Guo, J. Wang, L. Liu, Improved catalytic capability of mesoporous TiO_2 microspheres and photodecomposition of toluene, ACS Appl. Mater. Interfaces 2 (2010) 3134–3140.
[42] Y. Yang, D.S. Kim, Y. Qin, A. Berger, R. Scholz, H. Kim, M. Knez, U. Gösele, Unexpected long-term instability of ZnO nanowires “protected” by a TiO_2 shell, J. Am. Chem. Soc. 131 (2009) 13920–13921.
[43] J. Hou, C. Yang, Z. Wang, W. Zhou, S. Jiao, H. Zhu, In situ synthesis of <- ® phase heterojunction on Bi_2O_3 nanowires with exceptional visible-light photocatalytic performance, Appl. Catal. B Environ. 142-143 (2013) 504–511.
[44] J. Hou, Z. Wang, S. Jiao, H. Zhu, 3D $Bi_{12}TiO_{20}/TiO_2$ hierarchical heterostructure: synthesis and enhanced visible-light photocatalytic activities, J. Hazard. Mater 192 (2011) 1772–1779.
[45] R. Marschall, Semiconductor composites: strategies for enhancing charge carrier separation to improve photocatalytic activity, Adv. Funct. Mater 24 (2014) 2421–2440.
[46] R. Vinu, G.J.J. Madras, Environmental remediation by photocatalysis, J. Indian Inst. Sci. 90 (2010) 189–230.
[47] J. Hou, Z. Wang, C. Yang, W. Zhou, S. Jiao, H. Zhu, Hierarchically plasmonic Z-scheme photocatalyst of Ag/AgCl nanocrystals decorated mesoporous single-crystalline metastable $Bi_{20}TiO_{32}$ nanosheets, J. Phys. Chem. C 117 (2013) 5132–5141.
[48] S. Khanchandani, S. Kundu, A. Patra, A.K. Ganguli, Band gap tuning of ZnO/In_2S_3 core/shell nanorod arrays for enhanced visible-light-driven photocatalysis, J. Phys. Chem. C 117 (2013) 5558–5567.
[49] G.M. Clavier, J.L. Pozzo, H. Bouas-Laurent, C. Liere, C. Roux, C. Sanchez, Organogelators for making porous sol-gel derived silica at two different length scales, J. Mater. Chem. 10 (2000) 1725–1730.